Numerical simulation of propagation of solitary deformation waves in a compressible hyperelastic rod

Research Report Mech 293/08

Margit Vallikivi*, **Andrus Salupere***, **Hui-Hui Dai****

January 7, 2009

*Centre for Nonlinear Studies - CENS, Institute of Cybernetics at Tallinn University of Technology, Akadeemia tee 21, 12618, Tallinn, Estonia

**Department of Mathematics, City University of Hong Kong, 83 Tat Chee Avenue, Kowloon Tong, Hong Kong

Abstract

In this paper, propagation of axisymmetric deformation waves in circular cylindrical rods of compressible hyperelastic material is studied. Corresponding model equation that describes propagation of waves of moderate wave-length takes into account the coupling effect of the material nonlinearity and the geometric size of the rod. The model equation is integrated numerically under sech^2-type conditions making use of discrete Fourier transform based pseudospectral method. Numerical simulations are carried out over a wide range of material parameters. The analysis of the time-space behaviour of solutions demonstrate that in some domains of space of parameters single solitary wave solutions or trains of interacting solitons can be emerged from the initial localised pulses.

Keywords: Solitary waves, solitons, hyperelasticity, cylindrical rods

1 Introduction

Nonlinear axial-radial deformation waves in hyperelastic rods have been studied by many authors (see, for example, Samsonov [1], Porubov and Samsonov [2], Cohen and Dai [3], Dai and Huo [4], Dai and Fan [5]). These studies concentrated on weakly nonlinear long waves and only smooth solutions were considered. However, there are situations when the wave-length is only of moderate length. For these cases, it was argued in Dai [6] and Dai and Huo [7] that it is necessary to take into account the coupling effect of the material nonlinearity and the geometric size of the rod. With such a consideration, a new type of nonlinear equation with nonlinear dispersion terms was derived in Dai [6] and Dai and Huo [7] for a compressible Mooney-Rivlin material and a general compressible hyperelastic material respectively. The equation takes the following form:

$$u_\tau + \sigma_1 u u_\xi + \sigma_2 u_{\xi\xi\tau} + \sigma_3(2u_\xi u_{\xi\xi} + u u_{\xi\xi\xi}) = 0. \tag{1.1}$$

Here the dimensionless independent variables ξ and τ correspond to the moving frame, u is a quantity measuring the dimensionless deformation and σ_1, σ_2 and σ_3 are related to the material constants and the initial stretch of the rod. The last bracketed term represents the coupling effect of the material nonlinearity and the geometric size. It turns out that the parameter

$$\gamma = \frac{3\sigma_3}{\sigma_1\sigma_2} \tag{1.2}$$

plays certain important roles for the solutions of this equation. It was found in Dai and Huo [7] that for γ in five different intervals, $\gamma < 0$, $\gamma = 0$, $0 < \gamma < 3$, $\gamma = 3$ and $\gamma > 3$, this equation admits different travelling-wave solutions. In particular, it has the so-called non-smooth solitary shock wave (peakon or peaked solitary wave) and compacton solutions (see Dai and Huo [6] and Dai et al [7]). Due to its interesting properties, this equation has attracted a lot of attention recently. Constantin and Strauss [8] and Zhou [9] studied the stability of its solitary wave solutions. In Yin [10], the Cauchy problem was considered and it was shown that the equation has solutions that exist for indefinite times as well as solutions which blow up in finite time. Coclite et al [11] established existence of a strongly continuous semigroup of global weak solutions for any initial data from $H^1(\mathbb{R})$. Its integrability was studied by Ivanov [12] and it was shown that only when $\gamma = 1$ this equation is integrable. Despite that there are now many analytical studies on this equation, it appears that no numerical study has been done yet. In this paper, some initial-value problems of this equation are investigated numerically by a pseudospectral method. As it has been shown theoretically (see Dai and Huo [7] and Yin [10]) that the value of γ can influence the solutions greatly, here one purpose is to examine numerically how this parameter influences the solutions of the initial-value problems. Of particular interest is the mechanism by which it influences the appearance of solitary waves. Finally, we point out that Camassa and Holm [13] have derived equation

$$u_t + 2\kappa u_x + 3u u_x - u_{xxt} - 2u_x u_{xx} - u u_{xxx} = 0 \tag{1.3}$$

that describes shallow-water waves and is similar to equation (1.1). It is known that the Camassa–Holm equation (1.3) have peakon solutions for $\kappa = 0$. However, the parameter κ is proportional to the water depth and cannot be zero. Therefore such waves may not arise in shallow water.

The remaining of this paper is arranged as follows. In Section 2 the problem under consideration is stated and numerical method is introduced. Numerical results are discussed in Section 3 and conclusions are drawn in Section 4.

2 Statement of the problem and numerical method

In the present paper the propagation of localised initial pulses in hyperelastic rods (governed by equation (1.1)) is simulated numerically. For this reason the model equation (1.1) is integrated numerically under localised initial conditions

$$u(\xi, 0) = A\,\mathrm{sech}^2\,(B\xi)\,. \tag{2.1}$$

Here A is the amplitude and B is characterizing the width of the initial solitary pulse.

For numerical integration the discrete Fourier transform (DFT) based pseudospectral method (PsM) is used and therefore periodic boundary conditions

$$u(\xi,\tau)=u(\xi+2ml\pi,\tau),\quad l=\pm1,\pm2,\ldots,\quad m=1,2,3,\ldots \tag{2.2}$$

are applied ($2m\pi$ is the length of the space period). In a nutshell, the idea of the PsM is the following: space derivatives are found making use of DFT and for integration with respect to time standard ODE solvers are used [14, 15].

For periodic function $u=u(\xi,\tau)$ (with space period 2π) the DFT is introduced as follows:

$$U(k,\tau)=\mathrm{F}u=\sum_{j=0}^{N-1}u(j\Delta\xi,\tau)\exp\left(-\frac{2\pi ijk}{N}\right), \tag{2.3}$$

where N is the number of space-grid points, $\Delta\xi=2\pi/N$ – space step, i – imaginary unit, $k=0,\pm1,\pm2,\ldots,\pm\left(N/2-1\right),-N/2$ and F denotes the DFT. Now partial derivatives of u with respect to space coordinate x are

$$\frac{\partial^n u}{\partial\xi^n}=\mathrm{F}^{-1}\left[(ik)^n\mathrm{F}(u)\right], \tag{2.4}$$

where F^{-1} denotes the inverse DFT. Partial derivatives with respect to space coordinate are approximated by making use of formulae (2.4) thereby reducing a PDE to an ODE and allowing for straightforward integration with an ODE solver.

The usual PsM algorithm is derived for $u_t=\Phi(u,u_\xi,u_{2\xi},\ldots,u_{n\xi})$ type equations. However, equation (1.1) includes a mixed partial derivative and therefore in the present case one has to modify the standard PsM. First we rewrite the equation (1.1) in the form

$$\left(u+\sigma_2u_{\xi\xi}\right)_\tau=-\sigma_1uu_\xi-\sigma_3\left(2u_\xi u_{\xi\xi}+u_{\xi\xi\xi}\right) \tag{2.5}$$

and introduce a new variable

$$v=u+\sigma_2u_{\xi\xi}. \tag{2.6}$$

Making use of the DFT, the last expression can be rewritten in the form

$$v=\mathrm{F}^{-1}\left[\mathrm{F}\left(u\right)\right]+\sigma_2\mathrm{F}^{-1}\left[-k^2\mathrm{F}\left(u\right)\right]=\mathrm{F}^{-1}\left[\left(1-\sigma_2k^2\right)\mathrm{F}\left(u\right)\right]. \tag{2.7}$$

From the latter expression one can express the variable u and its space derivatives in terms of the new variable v:

$$u=\mathrm{F}^{-1}\left[\frac{\mathrm{F}\left(v\right)}{1-\sigma_2k^2}\right],\qquad \frac{\partial^n u}{\partial^n}=\mathrm{F}^{-1}\left[\frac{(ik)^n\,\mathrm{F}\left(v\right)}{1-\sigma_2k^2}\right]. \tag{2.8}$$

Finally, equation (2.5) can be rewritten in terms of variable v

$$v_t=-\sigma_1uu_\xi-\sigma_3\left(2u_\xi u_{\xi\xi}+u_{\xi\xi\xi}\right) \tag{2.9}$$

(variable u and all its space derivatives are calculated making use of formulae (2.8)). Therefore equation (2.9) can be considered as an ODE with respect to the variable v and could be integrated numerically making use of standard ODE solvers.

Goals of the current study are:

- to find numerical solutions for the proposed problem over a wide range of material parameters;
- to describe the time-space behaviour of the numerical solutions;
- to introduce different types of solutions;
- to examine the solitonic character of the solutions, i.e., to understand whether or not the emerged solitary waves can propagate at constant shapes and speeds and restore their amplitudes and speeds after interactions.

3 Numerical results and discussion

In the present Section two material models are considered for calculation of parameters σ_1, σ_2 and σ_3 for model equation (1.1). In the first case a compressible Mooney-Rivlin material is considered [6] and the Helmholtz free-energy function has the following form (see [16]):

$$\Phi = \frac{1}{2}\mu\left(\frac{1}{2}+\beta\right)(I_1-3)+\frac{1}{2}\mu\left(\frac{1}{2}-\beta\right)(I_2-3)+\frac{1}{2}\mu k\,(I_3-1)-\frac{1}{2}\mu\left(k+\frac{3}{2}-\beta\right)\ln I_3. \tag{3.1}$$

Here I_1, I_2 and I_3 are the principal invariants of the left Cauchy-Green deformation tensor. The elasticity parameter μ corresponds to the classical shear modulus, the dimensionless material constant β represents second-order effects [17], and k is a parameter for measuring the proportion of the two terms due to compressibility.

In the second case [7], the free-energy function is given in the form proposed by Hill [18]:

$$\begin{aligned} &\Phi = \sum_{n=1}^{3}\mu_n I(\alpha_n)+F(I_3), \qquad I(\alpha_n)=\frac{1}{\alpha_n}\left(l_1^{\alpha_n}+l_2^{\alpha_n}+l_3^{\alpha_n}-3\right), \\ &F(I_3)=\frac{\mu(1-2\alpha}{2\alpha}\left[I_3^{-\alpha/(1-2\alpha)}-1\right], \qquad \mu=\frac{1}{2}\sum_{i=1}^{3}\alpha_i\mu_i. \end{aligned} \tag{3.2}$$

Here l_i are the three principal stretches, I_3 is the third principal invariant, μ_i, α_i and α are material constants (α is playing a role similar to that of the Poisson ratio in classical theory).

3.1 First case

Firstly, numerical results are found for the parameters σ_1, σ_2 and σ_3, which are found as functions of $\mu > 0$, $-\frac{1}{2} \le \beta \le \frac{1}{2}$, λ and k (parameters of compressible Mooney-Rivlin material) according to [6]. Parameter λ characterises the initial state of the rod, $\lambda < 1$, $\lambda > 1$, $\lambda = 1$ represent that the rod is uniformly stretched, uniformly compressed and neutral, respectively. In current paper the uniformly stretched state ($\lambda < 1$) is studied.

When $\beta = \frac{1}{2}$ (and from what follows $\sigma_3 = \gamma = 0$, see [6, 16] for details), a compressible Mooney-Rivlin material becomes the so-called compressible neo-Hookean material. In this case equation (1.1) becomes

$$u_\tau + \sigma_1 u u_\xi + \sigma_2 u_{\xi\xi\tau} = 0. \tag{3.3}$$

Table 1: Values of parameters γ, σ_1, σ_2, σ_3 and B against λ, β, and k for the first case

λ	β	k	γ	σ_1	σ_2	σ_3	B	Type
0.8	0.50	1	0	1.081341	-0.015790	0	3.979100	1
0.8	0.49	1	0.016336	1.093797	-0.016131	-9.6E-5	3.936818	1
0.8	0.45	1	0.079351	1.146069	-0.017490	-0.000530	3.780719	1
0.8	0.42	1	0.124262	1.187949	-0.018504	-0.000910	3.675717	transition
0.8	0.39	1	0.167255	1.232255	-0.019511	-0.001340	3.579605	2
0.8	0.25	1	0.345070	1.475625	-0.024097	-0.004090	3.220956	2
0.9	0.39	1	0.091713	1.857347	-0.035593	-0.002021	2.650237	1
0.9	0.37	100	0.091877	1.950172	-0.065842	-0.003932	1.948587	1

This equation is the far-field equation for finite-length and finite-amplitude waves in a rod composed of a compressible neo-Hookean material and it is known as Benjamin-Bona-Mahony (BBM) equation. The solitary-wave solution for (3.3) is given as

$$u = A\,\mathrm{sech}^2\left[\frac{1}{2}\frac{1}{\sqrt{-\sigma_2}}\xi - \frac{1}{6}\frac{\sigma_1 A}{\sqrt{-\sigma_2}}\tau + s_0\right], \tag{3.4}$$

where s_0 is a phase constant [6].

The aim of this subsection is to solve equation (1.1) numerically for $|\sigma_3| << 1$ and to use the analytical solution of the BBM equation as the initial condition, i.e., B in (2.1) is considered to be given by expression (3.4):

$$B = \frac{1}{2}\frac{1}{\sqrt{-\sigma_2}}. \tag{3.5}$$

Remember, that for $\gamma = \sigma_3 = 0$ the model equation (1.1) reduces to the BBM equation (3.3). Numerical solutions are found for $0.5 < \lambda < 1$, $k = 1$, $\mu = 1$ (suggested by Dai [7]) and $\frac{1}{4} < \beta < \frac{1}{2}$. For these cases $0 < \gamma < 1$ and $|\sigma_3| << 1$. Calculations are carried out at space period 2π over time interval $0 \le \tau \le 500$.

Two main solution types are detected.

- Type 1 – solitary wave with a small-amplitude oscillating structure, $0 < \gamma < 0.094$.
- Type 2 – oscillating structure, $\gamma > 0.165$.

3.1.1 First solution type.

At first we consider values $\lambda = 0.8$ and $\beta = 0.49$. Corresponding values for σ_1, σ_2, σ_3 and γ are presented in Table 1. For the initial amplitude the value $A = 0.1$ is used. In Fig. 1 the profile of initial pulse and wave profiles at time moments $\tau = 100$ and $\tau = 500$ are shown. It can be seen, that the initial solitary wave slightly changes form in time, amplitude rises a little and a certain small-amplitude oscillating structure forms behind the solitary wave. The oscillations are quite small and do not affect the behaviour of the solitary wave considerably. The time-slice plot in Fig. 2 gives a good overview of the solution behaviour in time. One can say that the oscillating structure is quite localised in space and interacts

with the solitary wave (of the other space period) after certain time intervals. Amplitude curves in Fig. 3 clearly demonstrate that the solitary wave restores its height between such interactions and that each interaction produces additional oscillations. In this sense the solitary wave behaves like soliton.

When decreasing β and therefore increasing γ, the behaviour of the solution changes remarkably. In Figs. 4–6 solution for $\beta = 0.45$ is shown. Single wave profiles in Fig. 4 show that the wave profile narrows and heightens, at the same time stronger oscillations appear, compared to case $\beta = 0.49$ in Fig. 1. Time-slice plot in Fig. 5 demonstrates that the oscillating structure can be considered localised only before it interacts first time with the solitary wave. This interaction produces so strong additional oscillations that the solitary wave and the oscillating structure are in permanent interaction, at least for $\tau > 200$. Furthermore, the oscillating structure cannot be considered as localised entity anymore. The same circumstances are reflected in amplitude curves in Fig. 6. The amplitude of the solitary wave has nearly constant value only in the beginning of the interaction interval between $\tau \approx 50$ and $\tau \approx 125$, i.e., until the first interaction takes place. Later it oscillates about a certain level, because the solitary wave and the oscillating structure are in permanent interaction. Our analysis shows that notwithstanding the permanent interaction the solitary wave travels at constant speed. Comparing time-slice plots in Figs. 5 and 2 one can conclude, that for $\beta = 0.45$ the solitary wave travels faster than for $\beta = 0.49$.

For negative amplitude $A = -0.1$ the behaviour of the solution is slightly different. In Figs. 7–9 solution for $\beta = 0.45$ and $A = -0.1$ is shown. In Fig. 7 single wave profiles are given. The initial profile lowers and widens when oscillating structure is generated. The wave moves in the negative direction of the ξ-axis (cf. Figs. 5 and 8) and the speed is smaller for negative A (apparently due to the wider and lower shape of the solution). The first hump of the appearing oscillating structure is created on the positive side of the u-axis as it did for positive A (cf. Figs. 4 and 7). The oscillating structure becomes more relevant and as it moves in the opposite direction, it affects the amplitude of the solitary wave faster, so the amplitude starts to oscillate earlier than in case of $A > 0$ (cf. Figs. 6 and 9).

3.1.2 Second solution type

By decreasing β (γ increases, see Table 1), the behaviour of the solution changes. Here, solutions for $A > 0$ are discussed for $\beta = 0.39$ and $\lambda = 0.8$ (Table 1). This solution type can be detected if the parameter γ exceeds approximately value 0.165. The oscillating structure dominates, initial wave profile looses its form quickly and no solitary waves can be detected (see Fig. 10 where some wave profiles are presented). In Figs. 11 and 12 a typical time-slice plot and wave profile maxima against time for this type of solution are shown. The amplitude of the initial pulse decreases and the solution becomes an oscillating structure. By decreasing parameter β parameter σ_3 increases and the fourth term in equation (1.1) becomes more relevant, solution for smaller β looses its regular behaviour and becomes more and more chaotic. This can be observed by comparing solutions for $\beta = 0.39$ in Figs. 10–12 and for $\beta = 0.25$ in Figs. 13–15

3.1.3 Discussion

For $0.094 < \gamma < 0.165$, the numerical calculations brake down. This is the domain, where the transition from Type 1 to Type 2 is taking place. Before braking, the wave profile becomes very steep, as seen in Fig. 16.

Both types of solutions are for cases where $\gamma > 0$. For the fixed parameters $\mu = 1$ and $k = 1$ no small negative γ appear. When negative γ is found, parameter σ_2 has to be very small and due to the condition (3.5), the initial wave becomes too narrow for computations (with current space period, 2π). As the goal is to solve model equation with parameter γ slightly differing from zero, solutions for negative γ are not studied in this section.

The influence of the parameter k on the character of the solution is very weak. For instance for $k = 1$ and $k = 100$ the solutions are of the same type for fixed values of γ. As an example wave profiles for $k = 1$ and $k = 100$ with almost equal values of γ (see Table 1) are shown in Fig. 17 for $\tau = 0$ and $\tau = 100$.

For amplitudes of the initial pulse $A > 0.1$ the speed of the solitary wave and critical value (that defines the domain where the first solution type is realised) for parameter γ increase. In other words, for $A > 0.1$ the first solution type is attained in wider domain of parameter γ and emerged solitary waves propagate faster to the right.

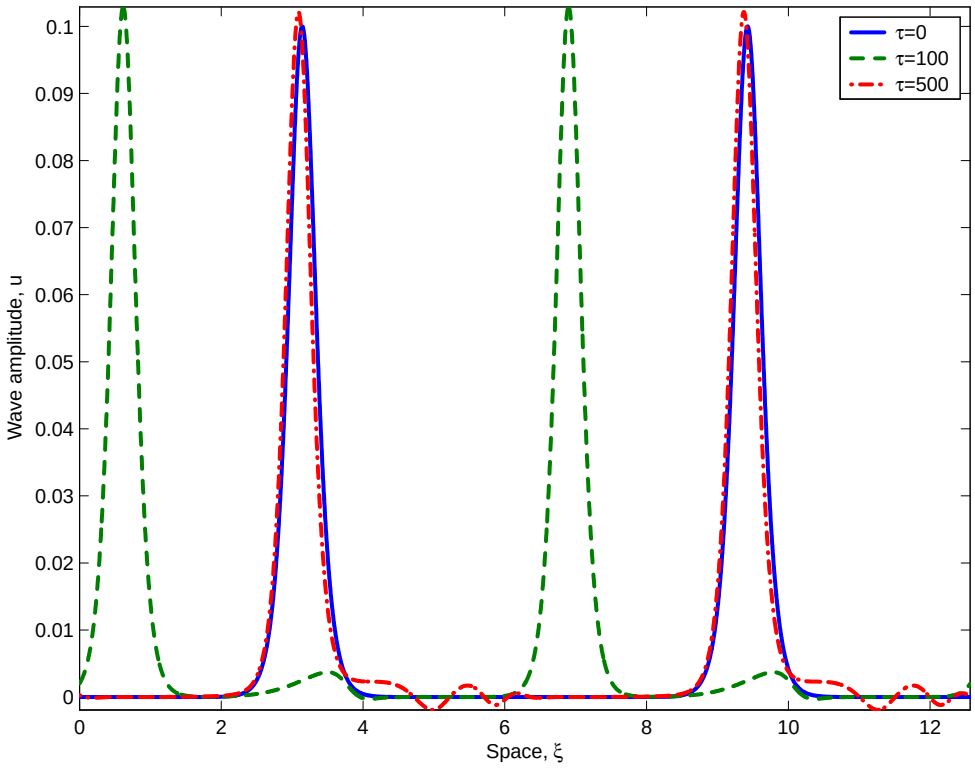

Figure 1: Single profiles over two space periods for $\lambda = 0.8$, $\beta = 0.49$, $A = 0.1$

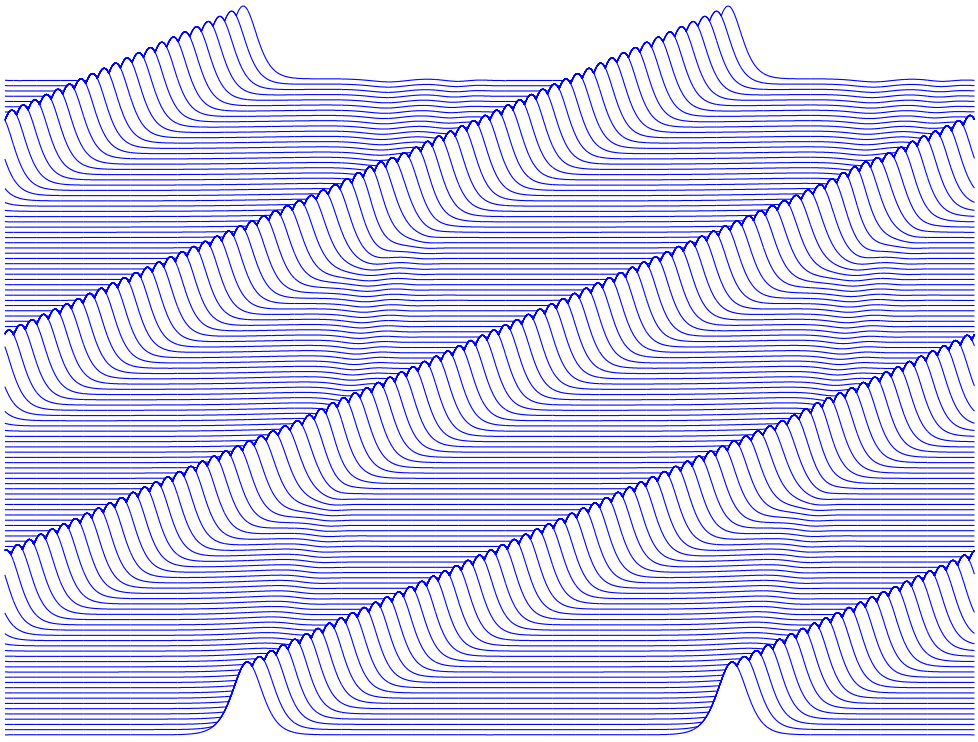

Figure 2: Time-slice plot over two space periods for $\lambda = 0.8$, $\beta = 0.49$, $A = 0.1$; $0 \leq \tau \leq 500$

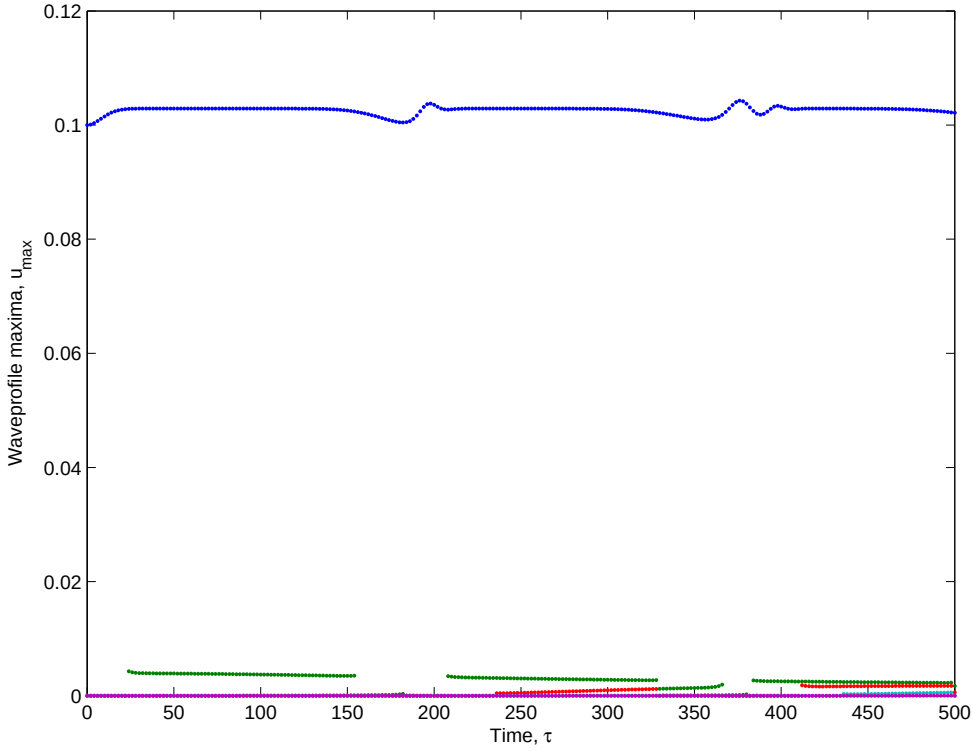

Figure 3: Wave profile maxima against time for $\lambda = 0.8$, $\beta = 0.49$, $A = 0.1$

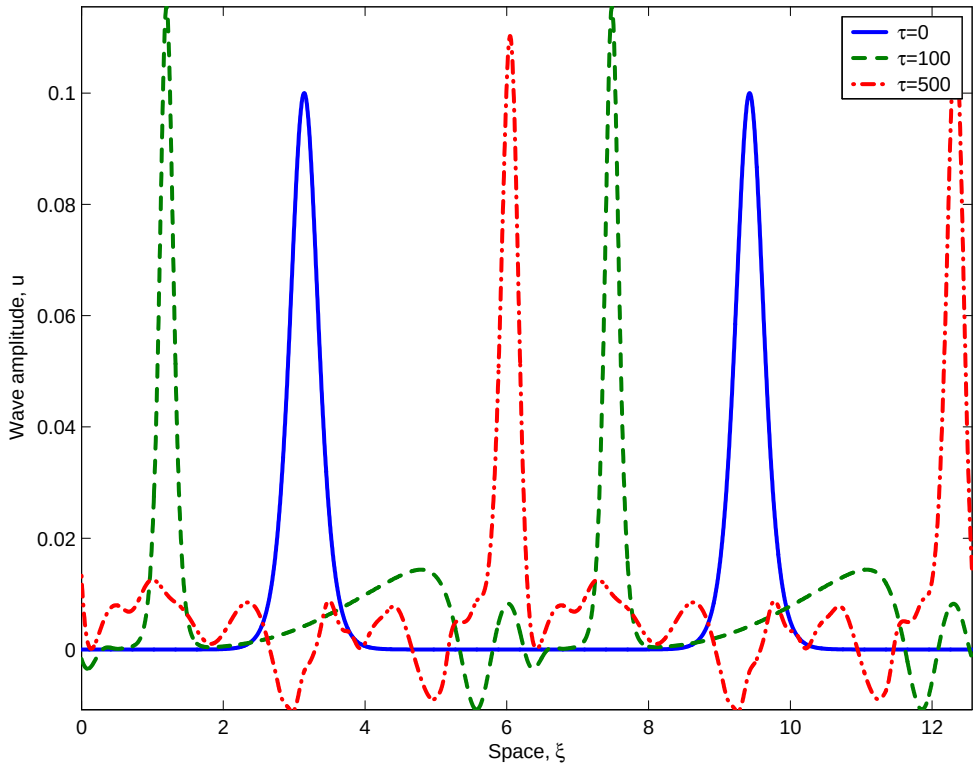

Figure 4: Single profiles over two space periods for $\lambda = 0.8$, $\beta = 0.45$, $A = 0.1$

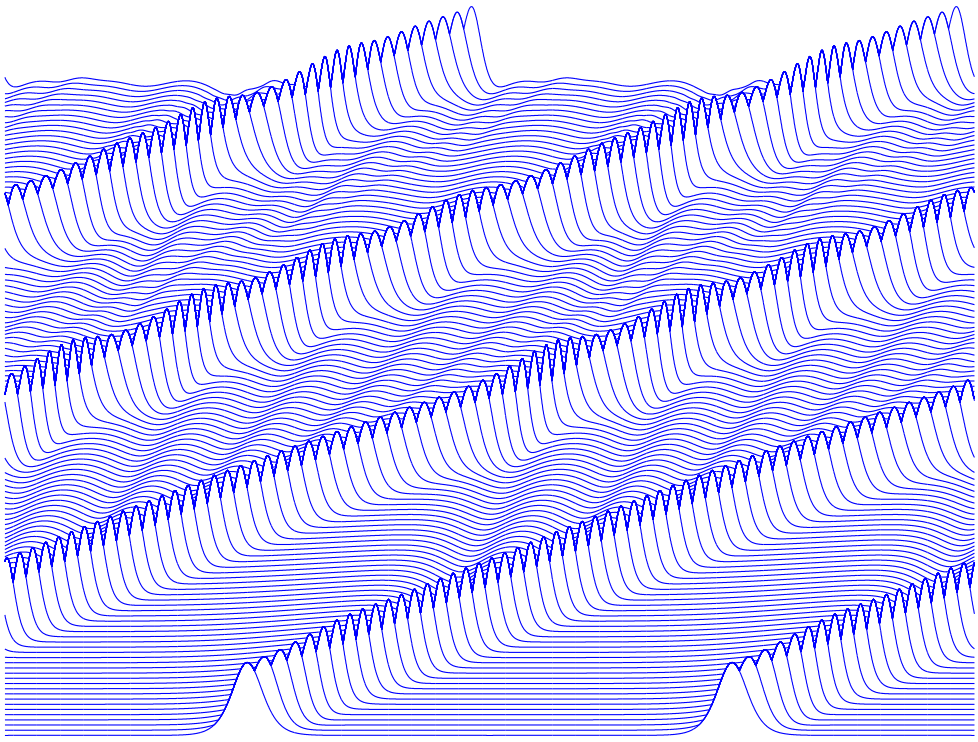

Figure 5: Time-slice plot over two space periods for $\lambda = 0.8$, $\beta = 0.45$, $A = 0.1$; $0 \leq \tau \leq 500$

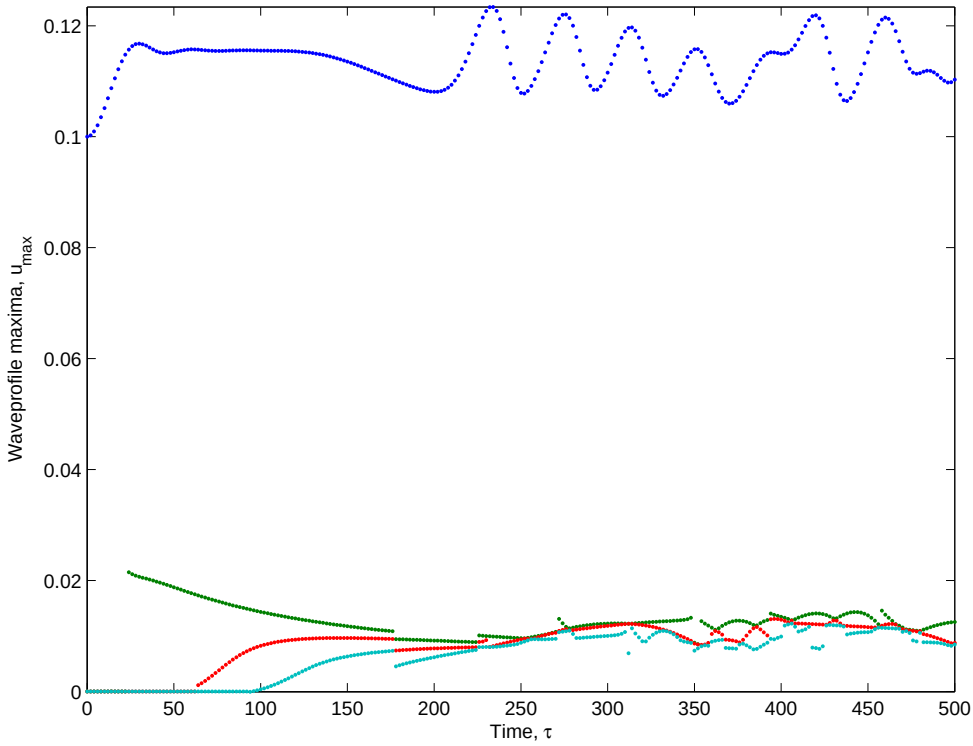

Figure 6: Wave profile maxima against time for $\lambda = 0.8$, $\beta = 0.45$, $A = 0.1$

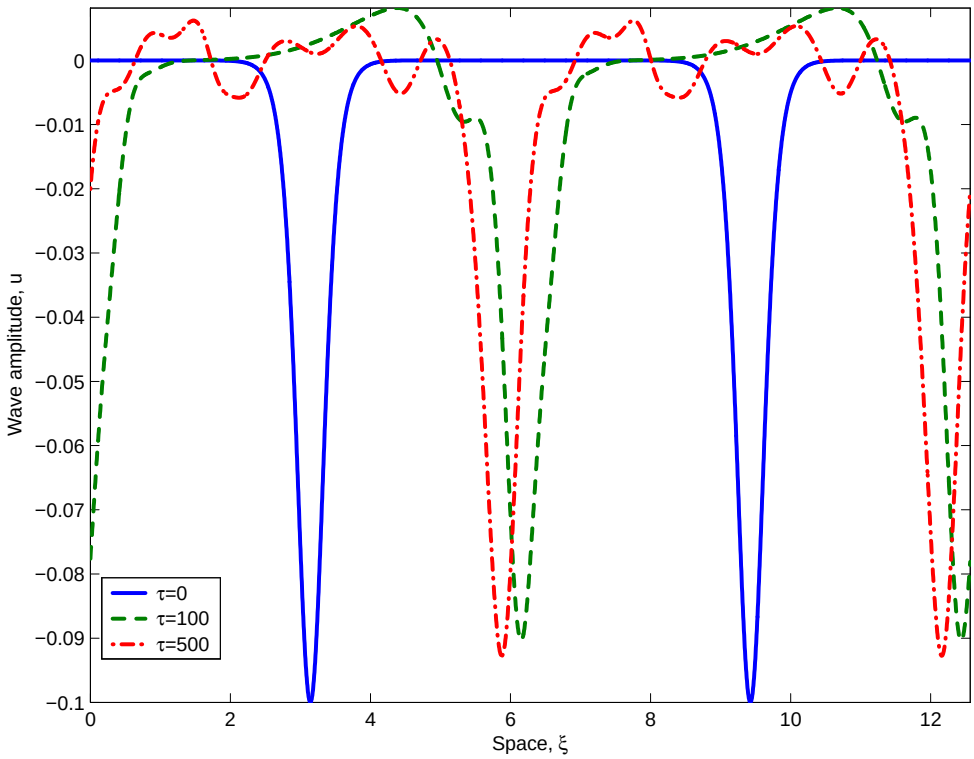

Figure 7: Single profiles over two space periods for $\lambda = 0.8$, $\beta = 0.45$, $A = -0.1$

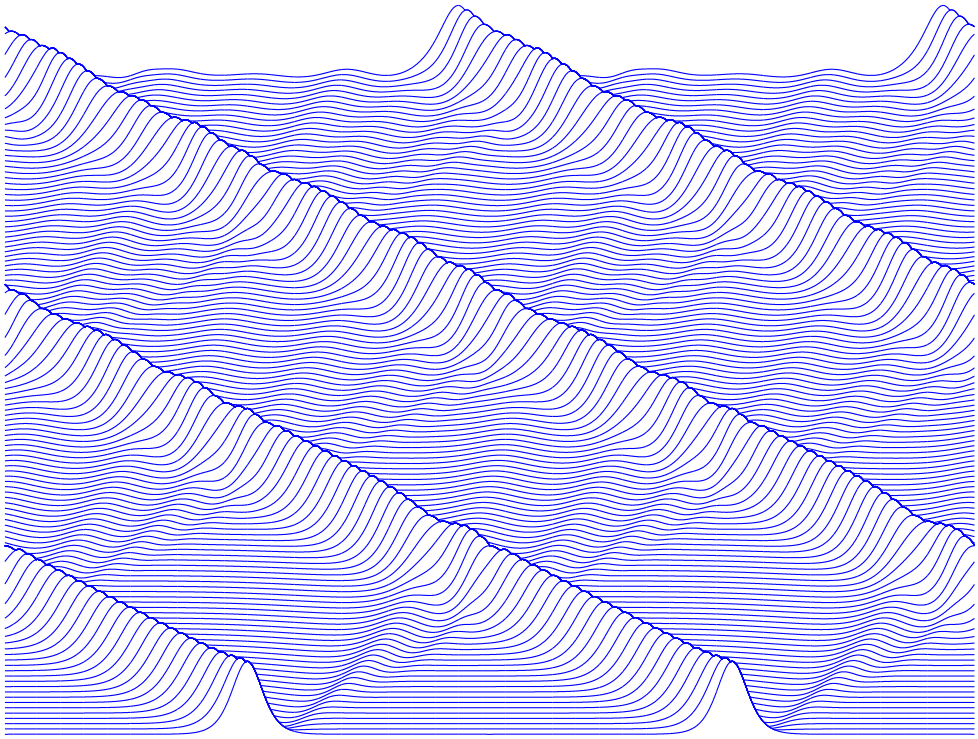

Figure 8: Time-slice plot over two space periods for $\lambda = 0.8$, $\beta = 0.45$, $A = -0.1$; $0 \leq \tau \leq 500$. Wave profiles have been inversed ($-u$ is considered instead of u for transparency).

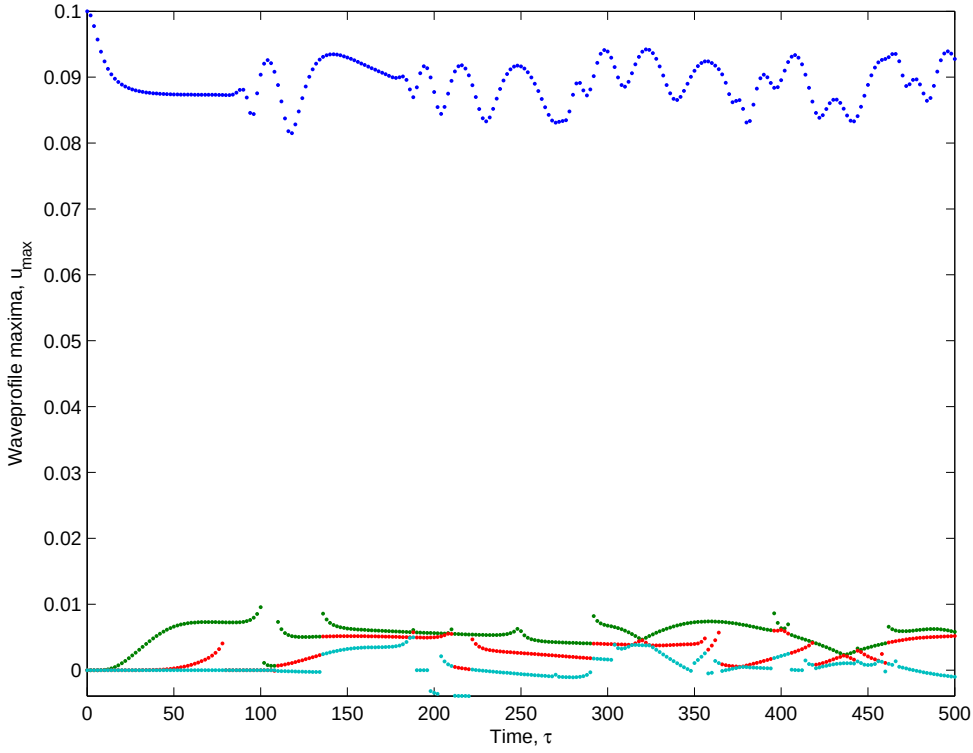

Figure 9: Maxima of $-u$ against time for $\lambda = 0.8$, $\beta = 0.45$, $A = -0.1$ ($-u$ is considered instead of u for transparency).

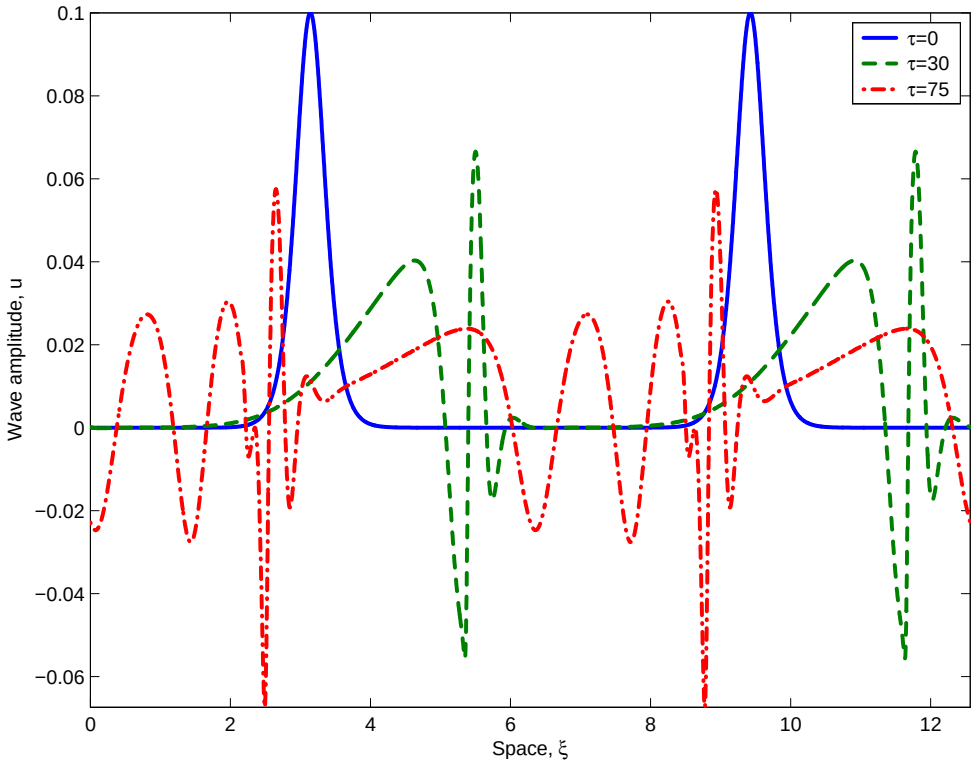

Figure 10: Single profiles over two space periods for $\lambda = 0.8$, $\beta = 0.39$, $A = 0.1$

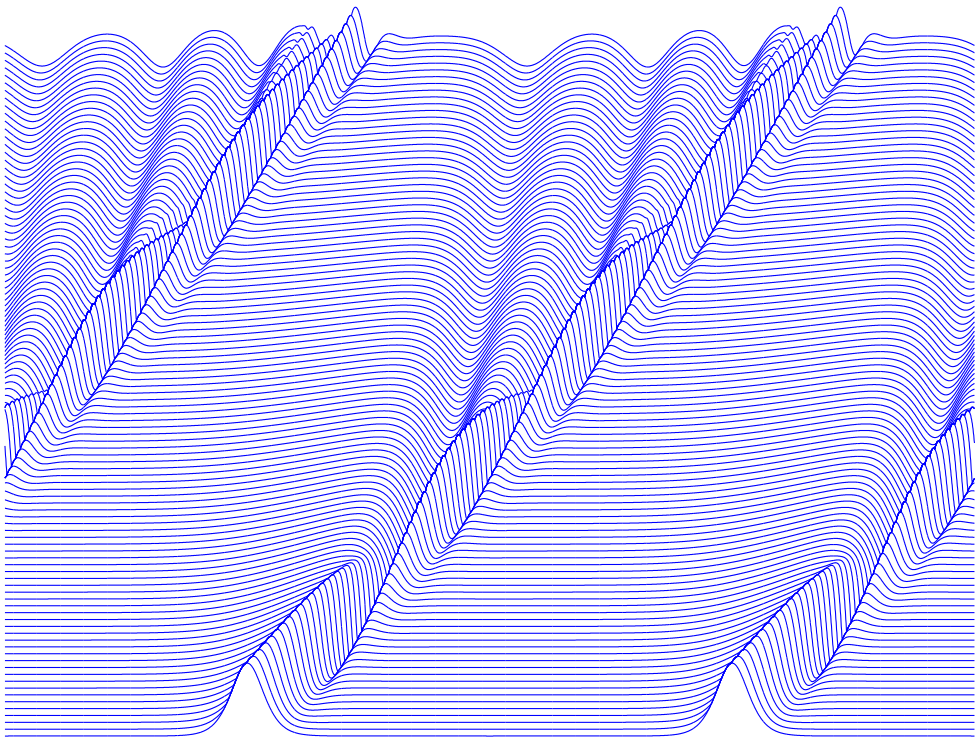

Figure 11: Time-slice plot over two space periods for $\lambda = 0.8$, $\beta = 0.39$, $A = 0.1$; $0 \leq \tau \leq 100$

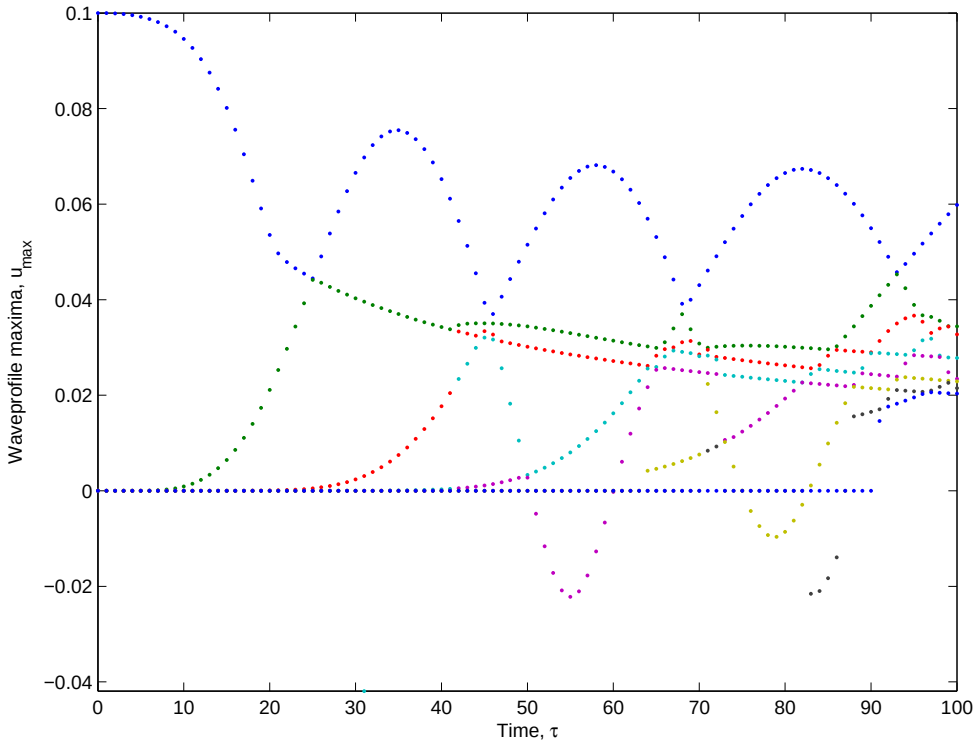

Figure 12: Wave profile maxima against time for $\lambda = 0.8$, $\beta = 0.39$, $A = 0.1$

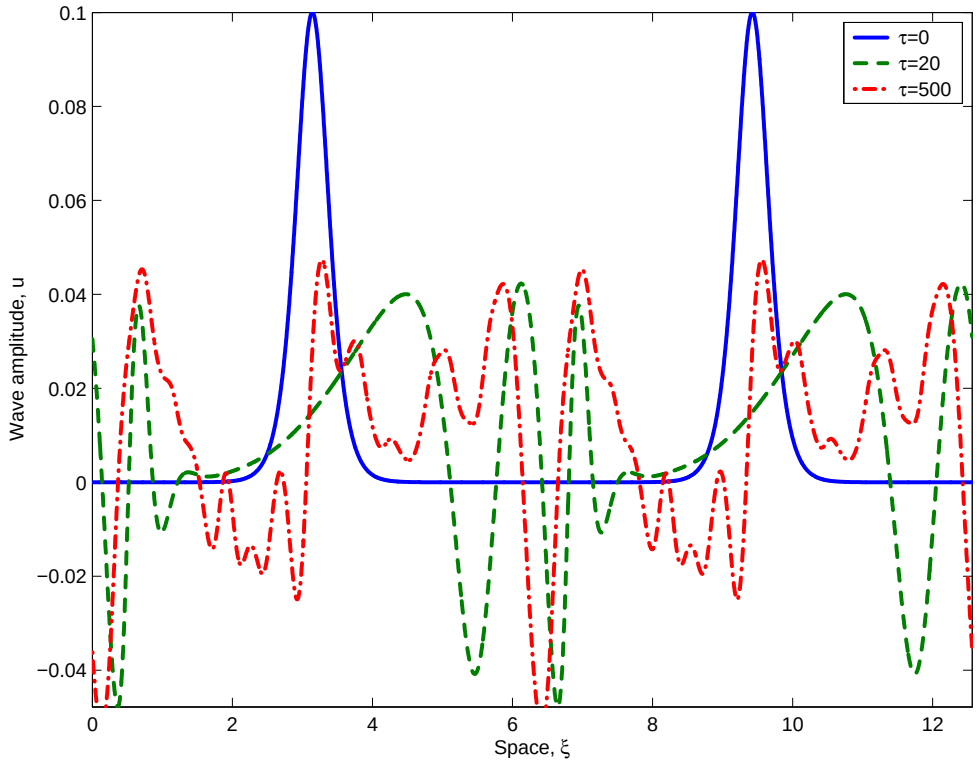

Figure 13: Single profiles over two space periods for $\lambda = 0.8$, $\beta = 0.25$, $A = 0.1$

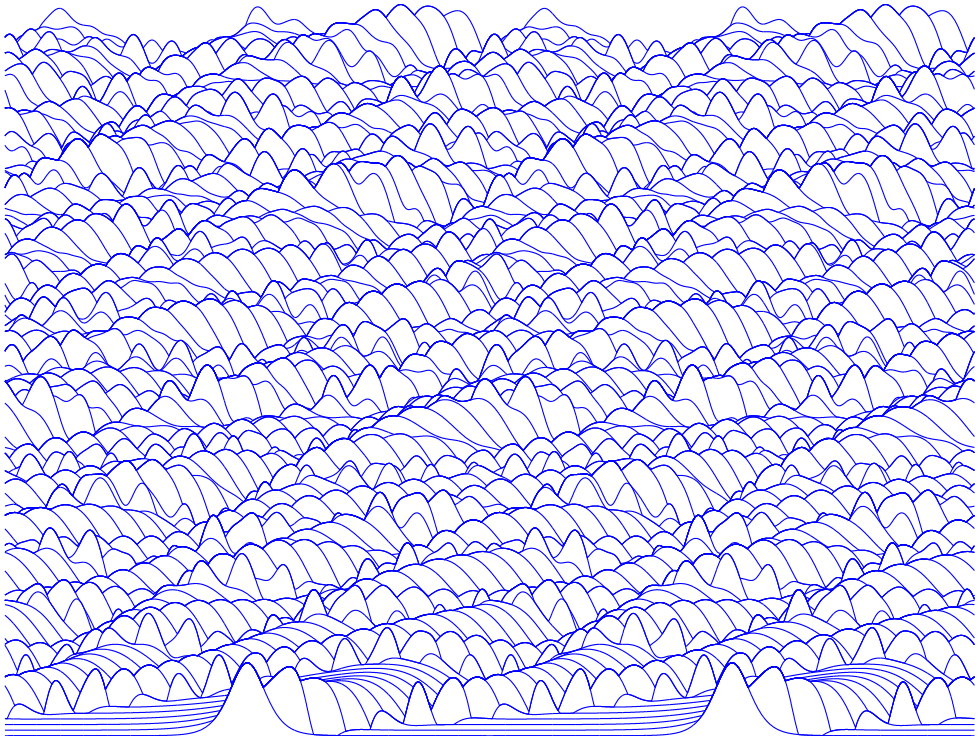

Figure 14: Time-slice plot over two space periods for $\lambda = 0.8$, $\beta = 0.25A = 0.1$; $0 \leq \tau \leq 500$

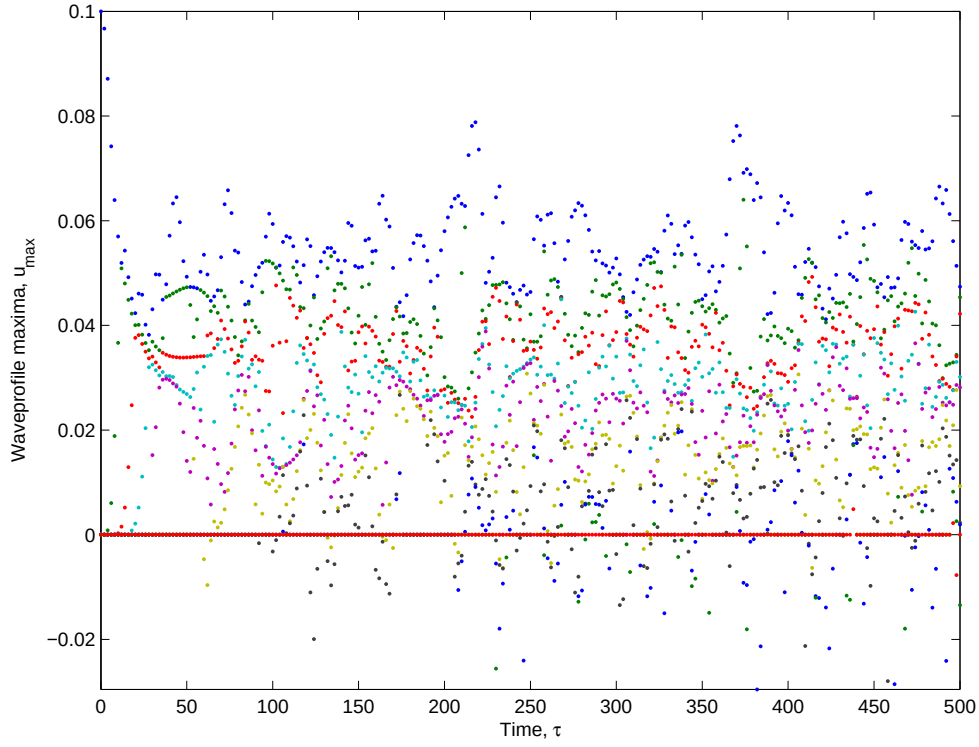

Figure 15: Wave profile maxima against time for $\lambda = 0.8$, $\beta = 0.25$, $A = 0.1$

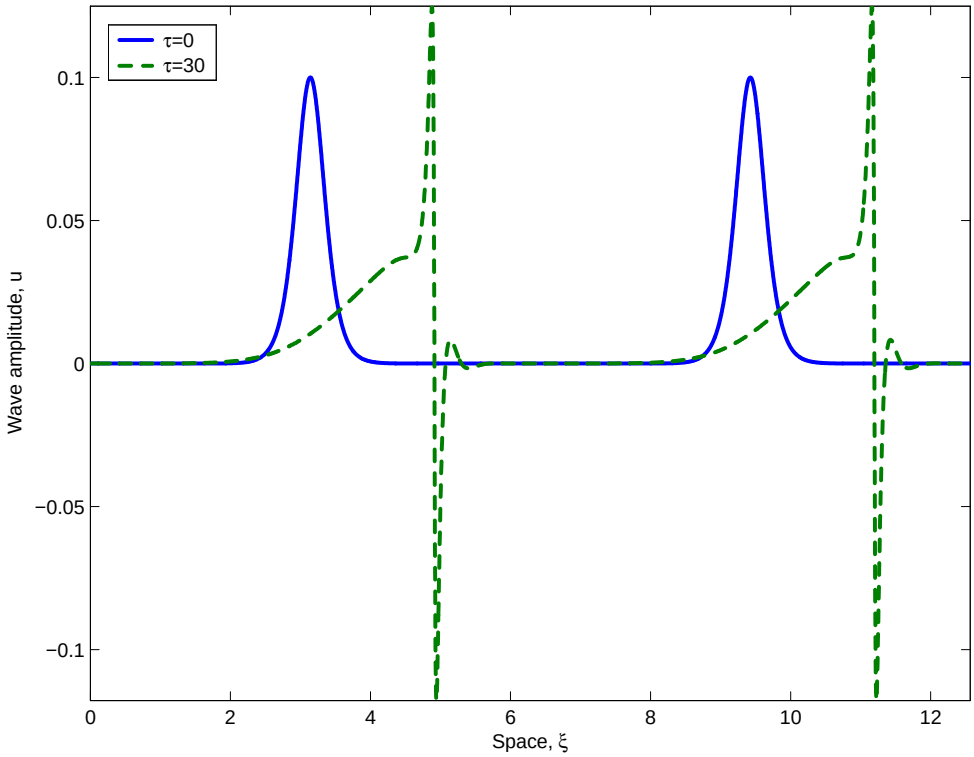

Figure 16: Single profiles over two space periods for $\lambda = 0.8$, $\beta = 0.42$, $A = 0.1$

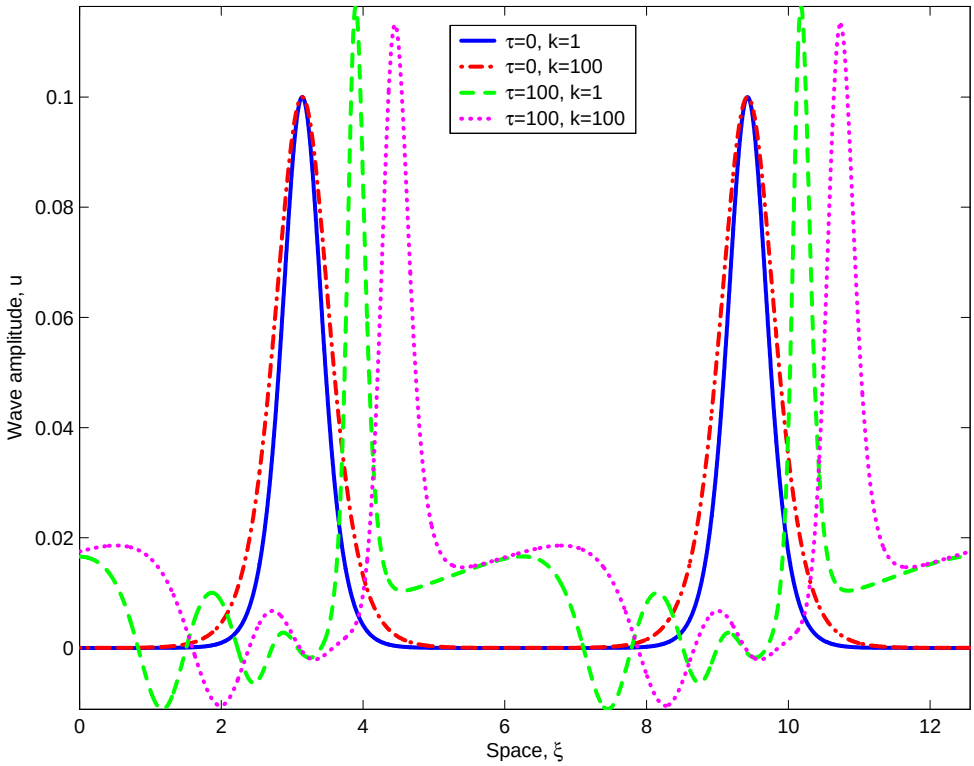

Figure 17: Single profiles over two space periods for $\lambda = 0.9$, $\beta = 0.39$, $k = 1$, $A = 0.1$ vs $\lambda = 0.8$, $\beta = 0.37$, $k = 100$, $A = 0.1$

3.2 Second case

In the second case, numerical results are found for values of parameters σ_1, σ_2 and σ_3 given in paper [7]. The values discussed in the current paper are presented in Table 2. The values for σ_2 are relatively small compared to values in Subsection 3.1 (see Table 1). In current subsection arbitrary values in the ranges $0.1 \leq A \leq 1.5$ and $0.5 \leq B \leq 3$ are considered for parameters of the initial pulse (2.1). Calculations are carried out at space period 40π and over time interval $0 \leq \tau \leq 1500$.

In case of $\gamma > 0$ no solitary wave solutions appear. The profile becomes very steep and something like a high-frequency harmonic oscillation is generated (see Fig. 18). Amplitudes decrease to a certain level and stay near it (Figs. 19 and 20).

In case of $\gamma < 0$ as typical type of solution, trains of solitons are detected. An example for $\gamma = -1.6460$ is shown in Figs. 21–23. The initial wave, with parameters $A = 0.1$ and $B = 0.5$, falls apart into a train of solitary waves with different height and amplitude, as one can see in Fig. 21. Time-slice plot in Fig. 22 demonstrates the behaviour of the solution in time, for $\tau = 1500$ the train consists of six solitary waves. One can see, that the speed of the waves in the train stays constant in time and higher waves travel faster than lower ones. Two emerging waves have higher amplitudes, than the initial solitary wave, and other ones lower, but the amplitudes stay constant in time (see Fig. 23).

When increasing B, the number of solitons in the train decreases and eventually, in the limit case only weak oscillations accompany the single solitary wave (in Fig. 24, the profiles are shown for $B = 3$). Fig. 25 shows the evolution of the single solitary wave solution in time. From wave maxima (Fig. 26) it can be seen that the amplitude stays constant. The weak oscillations after $\tau = 500$, are the result of interactions with the appearing oscillating structure (the tail). For smaller values of B the higher solitons in the train are higher than the initial wave. In case of bigger values of B (when only one solitary wave emerges) the amplitude of the propagating solitary wave is lower than that of the initial wave. Such a phenomenon is called selection — the shape of the initial wave is modified in a way to be more appropriate to the actual solution of the equation. In other words, selection means that during propagation the amplitude and velocity of an initial solitary wave tend to the finite values prescribed by the equation coefficients (see [19, 20, 21, 22] for details). By further increasing of B, the initial wave becomes so narrow, that computational algorithm fails.

For greater values of $|\gamma|$, for example for $\gamma = -4.8910$ the behaviour of the solution is similar — train of solitons evolve (Figs. 27–29). Here again it can be seen from wave profile maxima against time in Fig. 29, that the amplitudes reach a certain value and then stay practically constant. For greater $|\gamma|$ the number of solitons is smaller (from

Table 2: Values of parameters γ, σ_1, σ_2 and σ_3 for the second case

γ	σ_1	σ_2	σ_3
3.4174	0.7957	-0.0032	-0.0029
-1.6460	-0.7205	-0.0026	-0.0010
-4.8910	-0.3302	-0.0030	-0.0016
-29.4760	-0.0650	-0.0030	-0.0019

Figs. 21 and 27 it can be seen that for $\tau = 1500$ the number of solitons in the train is six and three, accordingly). In general (for all the sets of parameters given in [7]) it can be concluded, that the number of solitons in the train is determined by σ_2 — by decreasing the absolute value $|\sigma_2|$, the number of solitons increases. From model equation (1.1) it can be seen, that σ_2 controls the strength of the dispersion. Therefore, as in case of the celebrated KdV equation, for weaker dispersion the number of emerging solitons is higher. At the same time, the speeds of emerged solitary waves are depending on σ_1 — when the value of $|\sigma_1|$ is increased, the propagation speed of the highest solitons increases (cf. Figs. 22 and 28). As σ_1 is the coefficient of the nonlinearity in equation (1.1), one can conclude that the stronger the nonlinearity the faster the highest solitons propagate.

The amplitude A of the initial pulse also plays an important role in the behaviour of the solution. For higher initial pulses the train of solitons emerges faster and with greater number of solitons (see Figs. 30–32). In Fig. 30 the profile is given for $\tau = 600$ when the train of solitons has already been formed, i.e. just before interactions between solitons from neighbour space periods start to take place. From time-slice plot in Fig. 31 and wave profile maxima against time in Fig. 32 the time-space behaviour of the solution can be observed. The interactions are practically elastic, the amplitude of higher waves decreases and the amplitude of lower waves increases during the interactions. After interactions the amplitudes change back to the values they had before interactions.

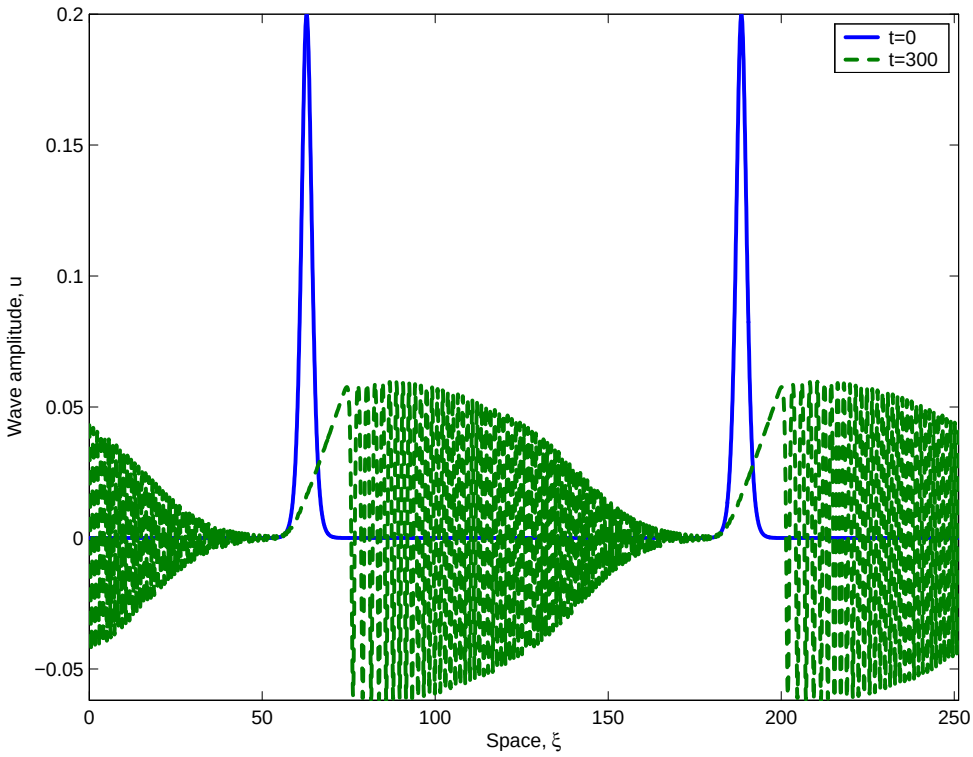

Figure 18: Single profiles over two space periods for $\gamma = 3.4174$, $A = 0.1$, $B = 0.5$

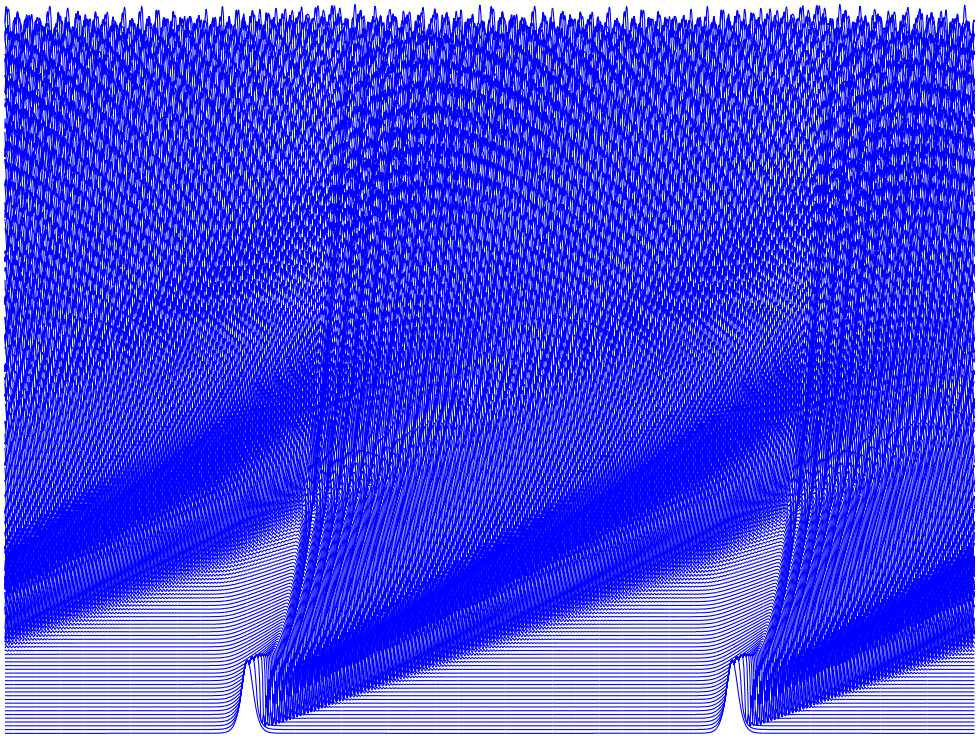

Figure 19: Time-slice plot over two space periods for $\gamma = 3.4174$, $A = 0.1$, $B = 0.5$; $0 \leq \tau \leq 1500$

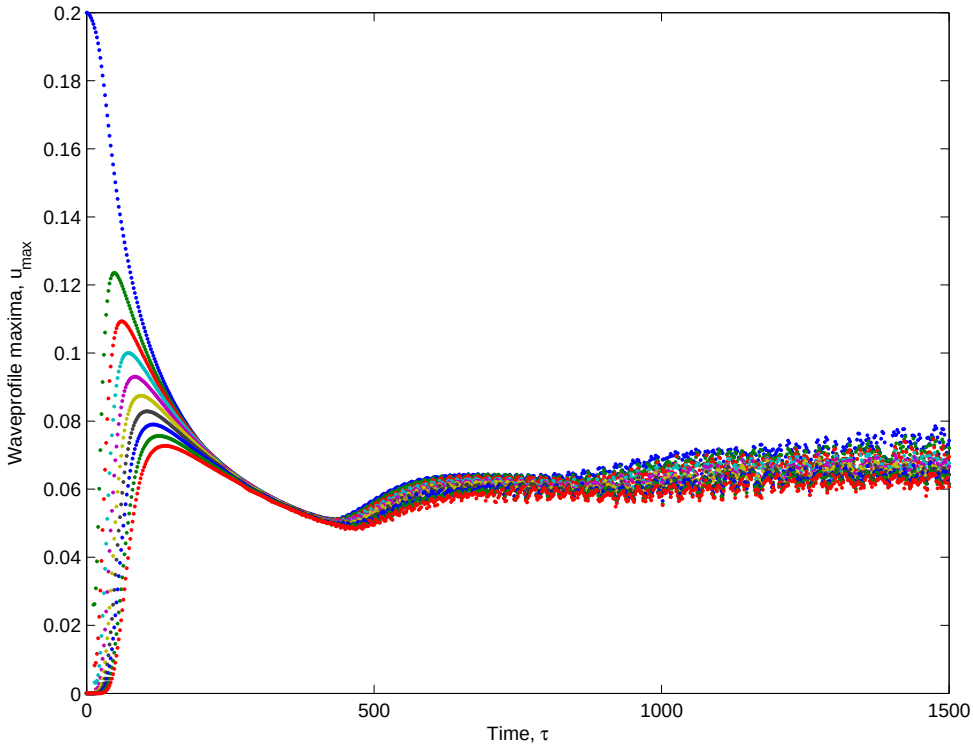

Figure 20: Wave profile maxima against time for $\gamma = 3.4174$, $A = 0.1$, $B = 0.5$

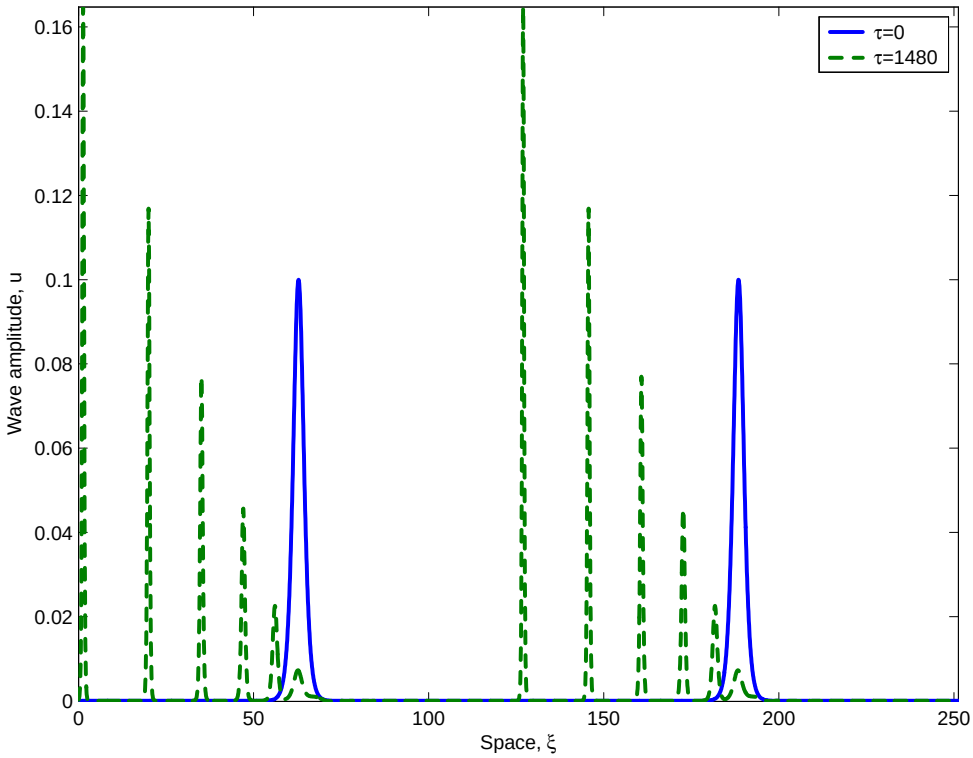

Figure 21: Single profiles over two space periods for $\gamma = -1.6460$, $A = 0.1$, $B = 0.5$

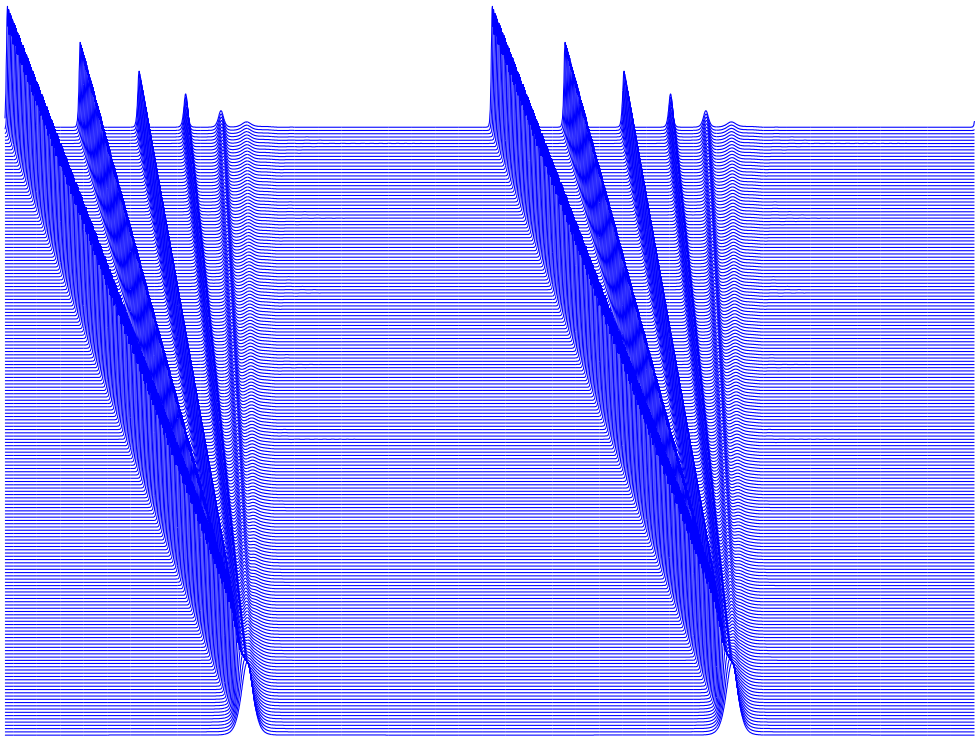

Figure 22: Time-slice plot over two space periods for $\gamma = -1.6460$, $A = 0.1$, $B = 0.5$; $0 \leq \tau \leq 1500$

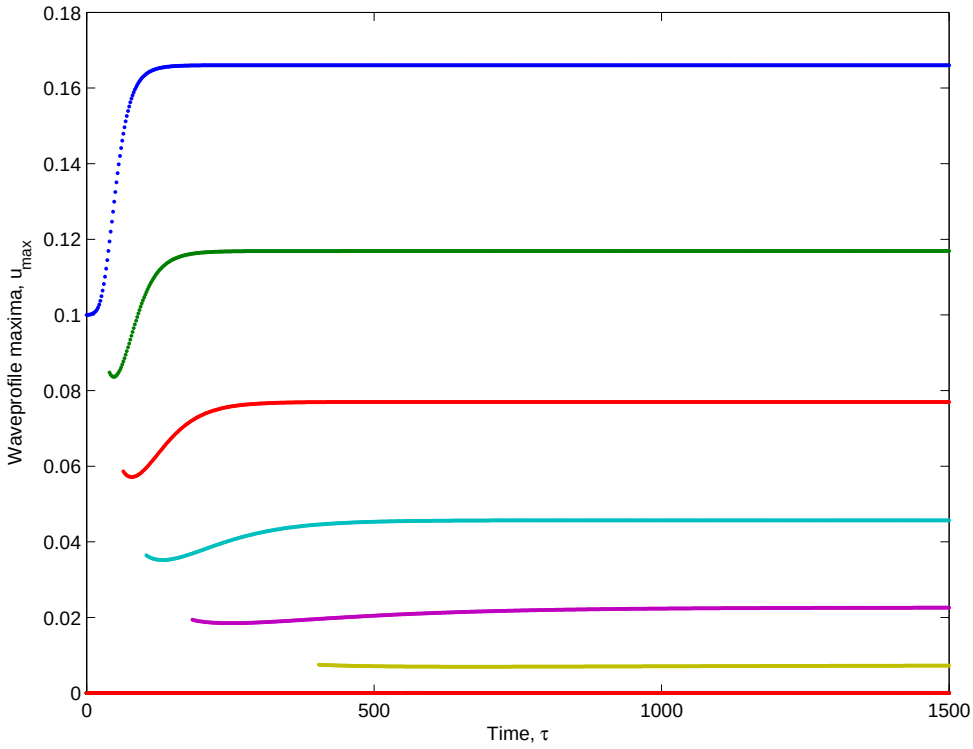

Figure 23: Wave profile maxima against time for $\gamma = -1.6460$, $A = 0.1$, $B = 0.5$

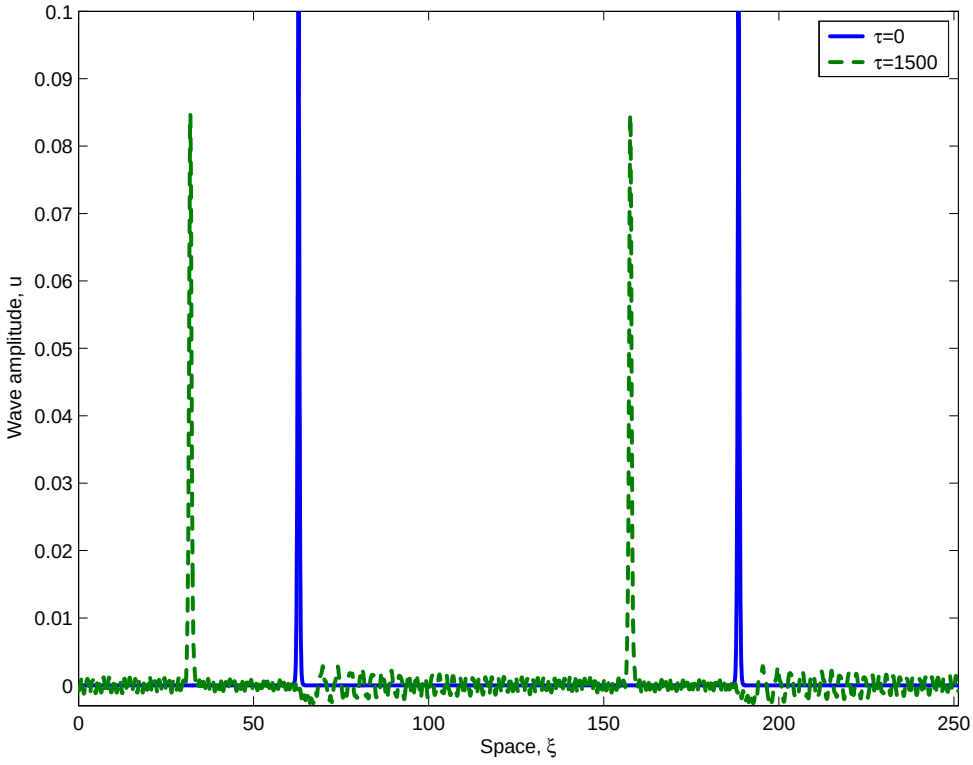

Figure 24: Single profiles over two space periods for $\gamma = -1.6460$, $A = 0.1$, $B = 3$

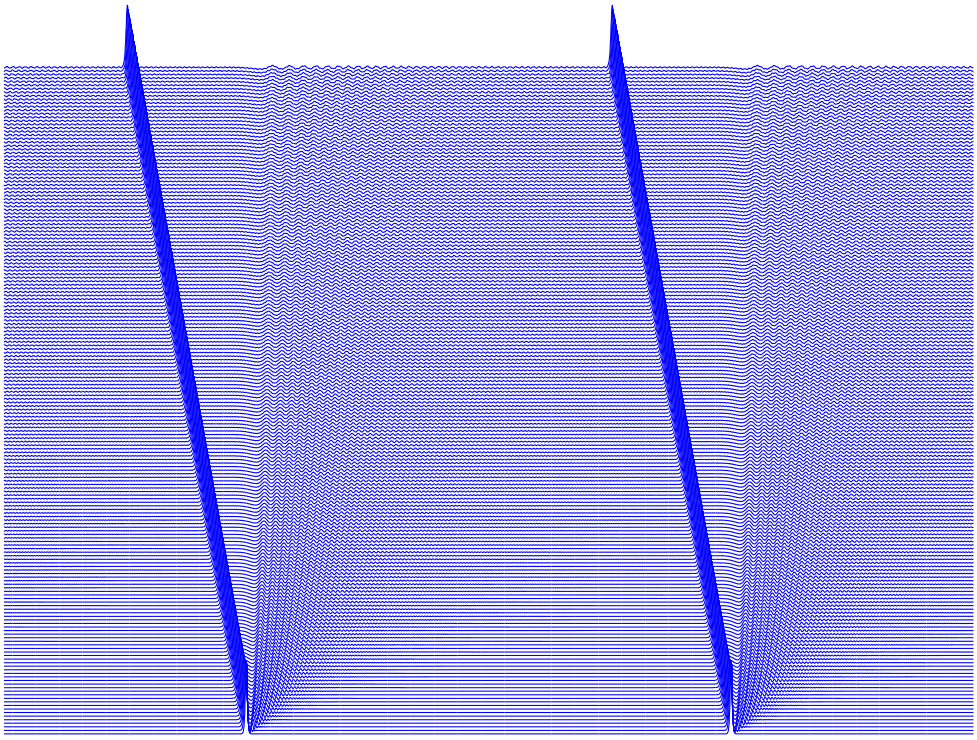

Figure 25: Time-slice plot over two space periods for $\gamma = -1.6460$, $A = 0.1$, $B = 3$; $0 \leq \tau \leq 1500$

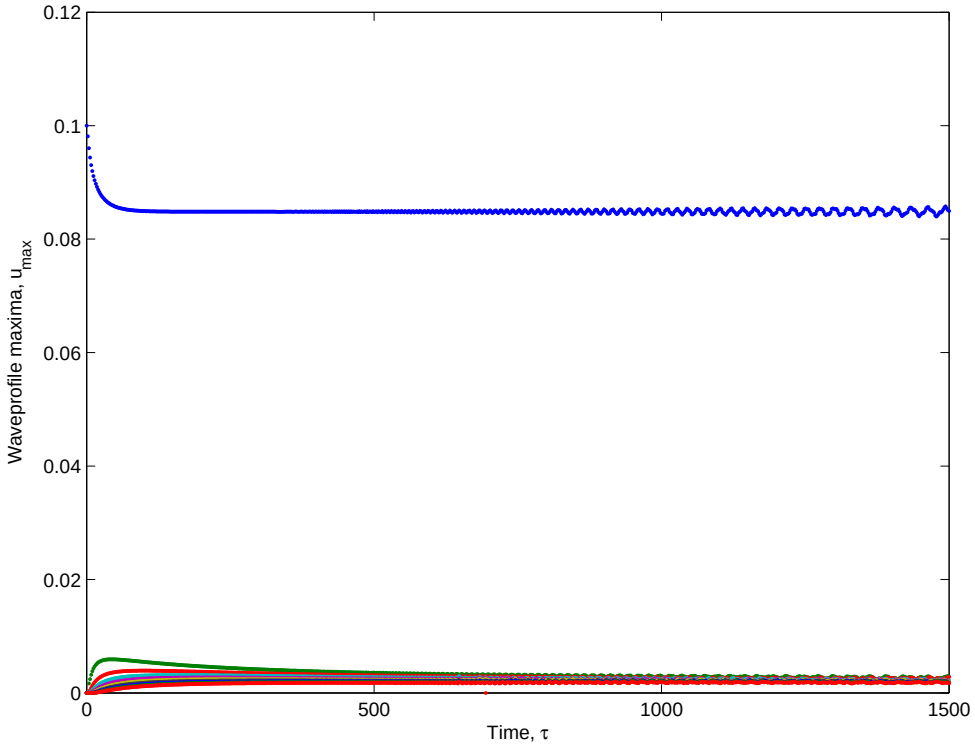

Figure 26: Wave profile maxima against time for $\gamma = -1.6460$, $A = 0.1$, $B = 3$

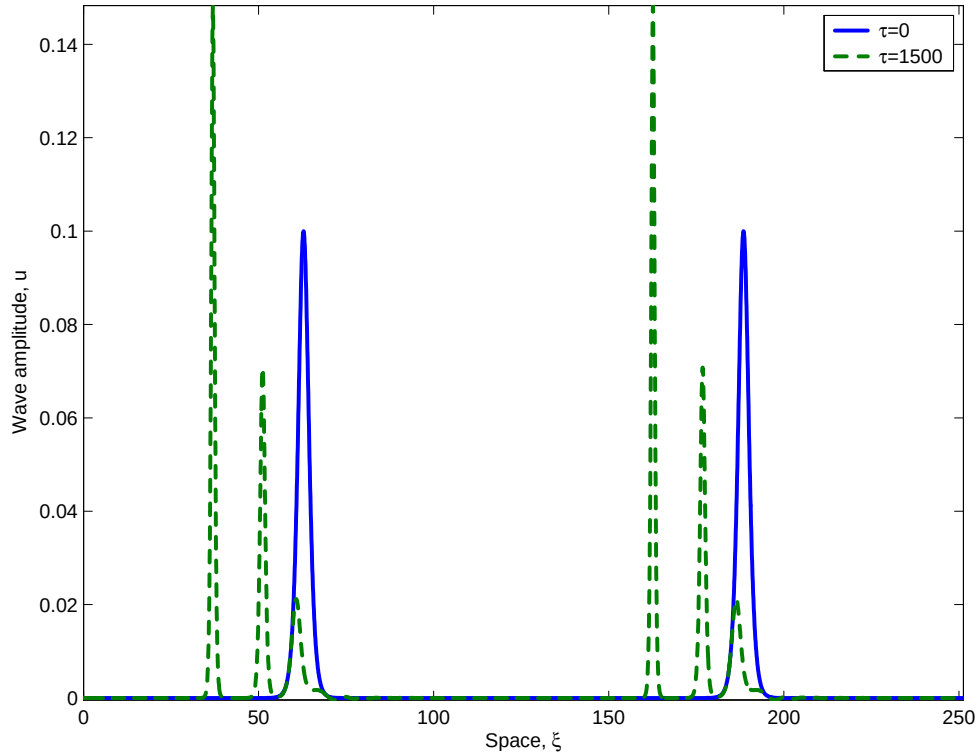

Figure 27: Single profiles over two space periods for $\gamma = -4.8910$, $A = 0.1$, $B = 0.5$

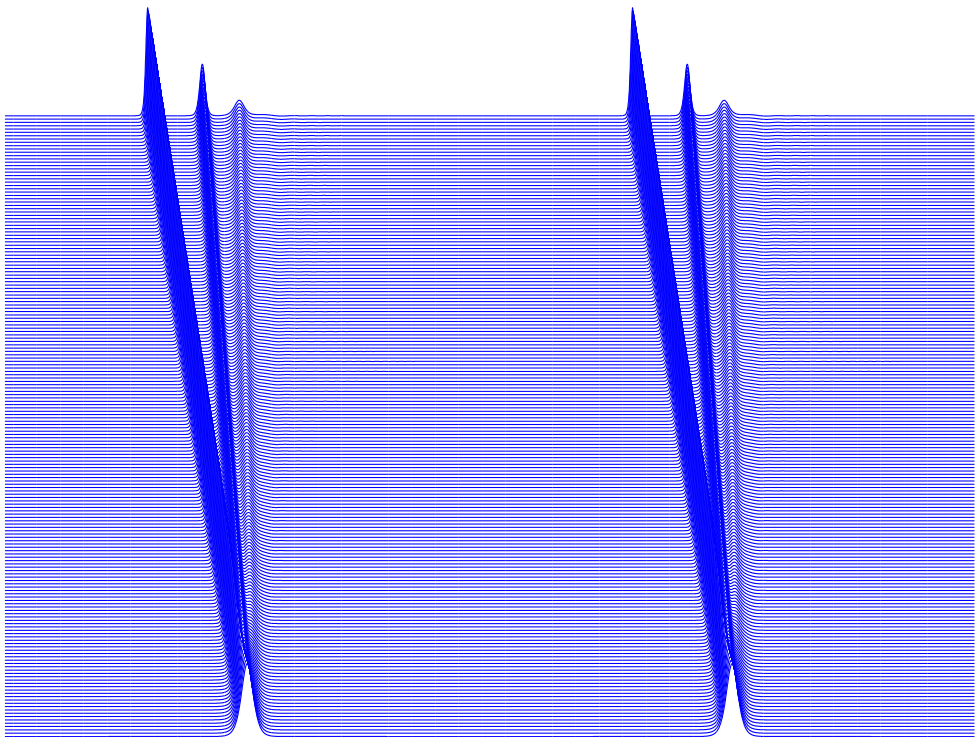

Figure 28: Time-slice plot over two space periods for $\gamma = -4.8910$, $A = 0.1$, $B = 0.5$; $0 \leq \tau \leq 1500$

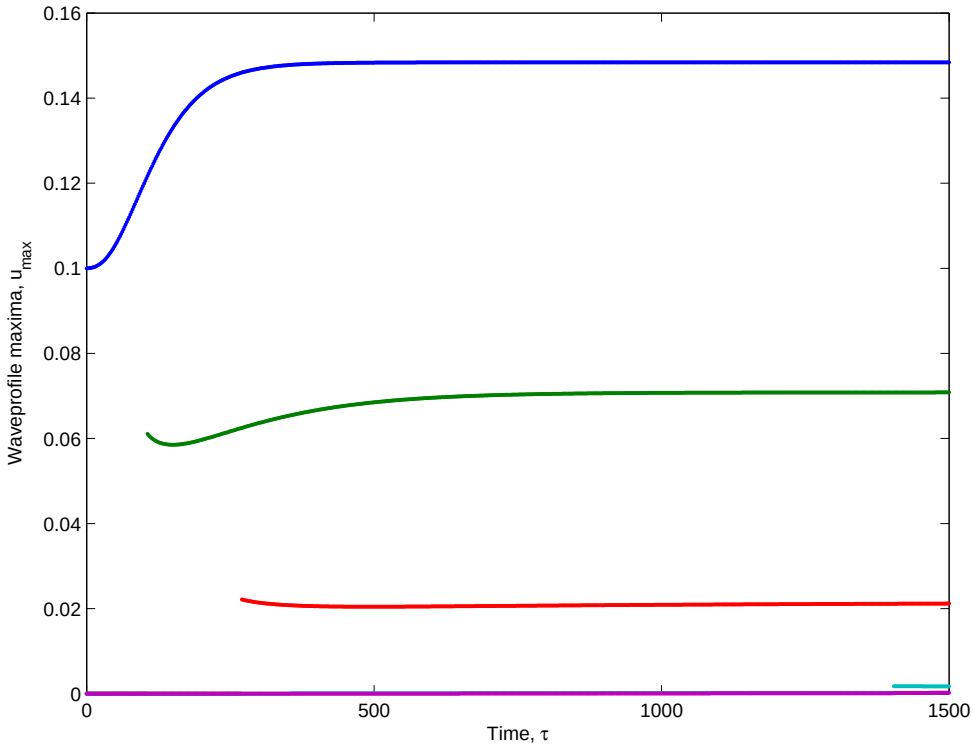

Figure 29: Wave profile maxima against time for $\gamma = -4.8910$, $A = 0.1$, $B = 0.5$

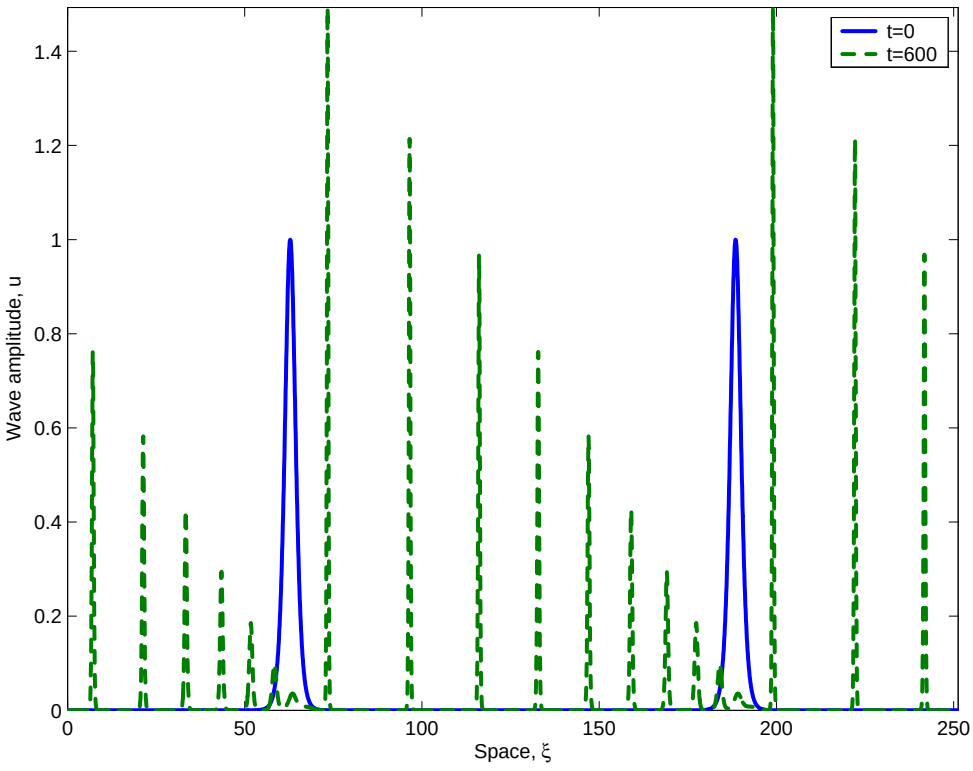

Figure 30: Single profiles over two space periods for $\gamma = -4.8910$, $A = 1$, $B = 0.5$

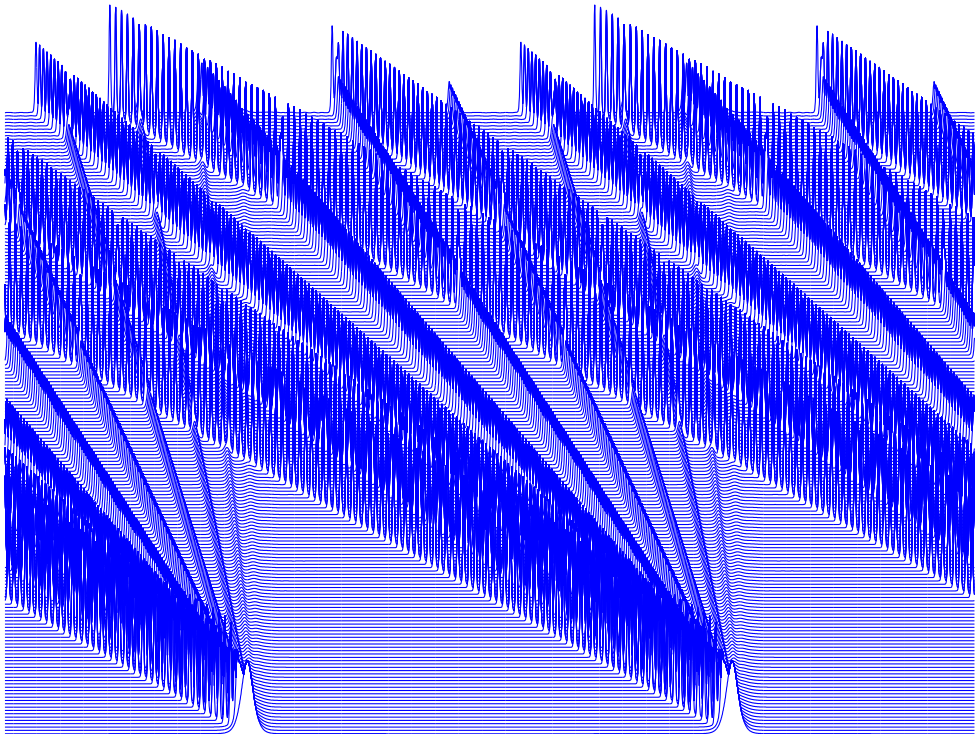

Figure 31: Time-slice plot over two space periods for $\gamma = -4.8910$, $A = 1$, $B = 0.5$; $0 \leq \tau \leq 1500$

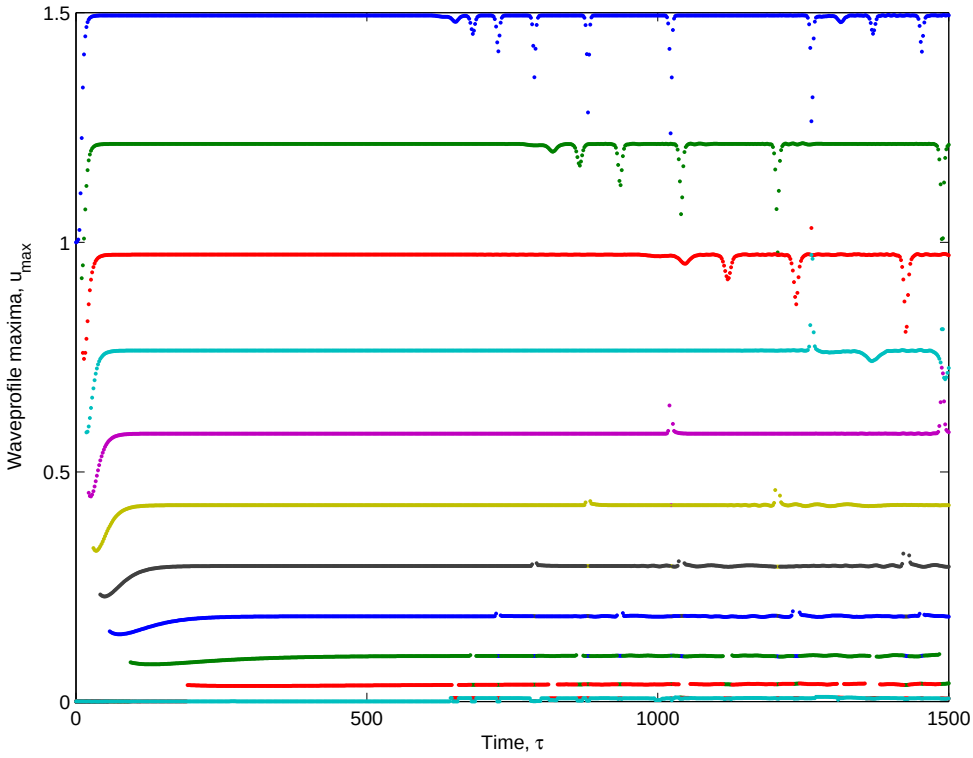

Figure 32: Wave profile maxima against time for $\gamma = -4.8910$, $A = 1$, $B = 0.5$

4 Conclusions

In the present paper equation (1.1) is applied for numerical simulation of propagation of deformation waves in a compressible hyperelastic rod. Numerical experiments are carried out for two cases. In the first case: (i) material parameters σ_i, $i = 1, 2, 3$ are calculated according to paper [6]; (ii) $|\sigma_3| << 1$ and $0 < \gamma < 1$ are considered; and (iii) the analytical solution of BBM equation — (2.1) with (3.5) — is used for the initial condition for the equation (1.1). In the second case: (i) values for material parameters σ_i, $i = 1, 2, 3$ are taken from paper [7]; (ii) parameter γ is not restricted to be $0 < \gamma < 1$; and (iii) arbitrary values of A and B is used for initial condition (2.1).

Main results:

- In the first case two main solution types are detected. The type is defined by values of parameter γ and the initial pulse parameters A and B. For initial amplitude $A = 0.1$ solitary wave (with small amplitude oscillating structure) is found to emerge for $0 < \gamma < 0.094$. For $A > 0.1$ solitary waves emerge in wider domain of parameter $\gamma > 0$.

- In the second case different solution types are detected for $\gamma < 0$ and for $\gamma > 0$. For $\gamma > 0$ the character of solution is solitonic — train of solitons emerges from the initial solitary wave.

- Dai and Huo [7] studied the existence of travelling wave solutions for equation (1.1). Different solution types were found for $\gamma < 0$, $0 < \gamma < 3$ and $\gamma > 3$. However, in numerical results no difference appeared, whether γ was bigger or smaller than 3 and only difference between positive and negative γ can be observed. By Dai and Huo [7], solitary wave solution can exist when conditions

$$\gamma < 0, \qquad 0 < A < (1 - 3/\gamma)V, \tag{4.1}$$

$$0 < \gamma < 3, \qquad 0 < A < \frac{1}{2}(3/\gamma - 1)V, \tag{4.2}$$

$$\gamma > 3, \qquad -\frac{1}{2}(1 + 3/\gamma)V < A < 0, \tag{4.3}$$

  are satisfied. However, in numerical experiments solitary waves emerge notwithstanding whether or not the conditions (4.1)–(4.3) are satisfied.

  It should be noted that in Dai and Huo [7] "exact" travelling-wave solutions (which include the single-solitary-wave solution without an oscillatory tail attached with it) in an infinite domain were studied. It also should be pointed out that multi-solitary waves are not "exactly" travelling waves as different solitary waves travel with different speeds. In the present work, numerical studies are carried out in a bounded domain with periodic conditions. When the numerical solutions of initial-value problems give solitary-wave type profiles, they are either in the form of a solitary wave with some oscillatory parts (although the amplitudes could be very small) or in the form of multi-solitary waves. Since in both cases they are not the "exact" travelling waves, the present results do not contradict with those findings in Dai and Huo [7]. Rather, the numerical solutions once again reveal that the parameter γ can greatly influence the solutions, which is in agreement with those results in Dai and Huo [7].

Acknowledgment

Authors of this paper thank Professor Jüri Engelbrecht for helpful discussions. The research was partially supported by Estonian Science Foundation Grant No 7035 (A.S. and M.V.) and EU Marie Curie Transfer of Knowledge project MTKD-CT-2004-013909 under FP 6 (A.S.). One of the authors (H.-H.D.) acknowledges the support of a grant from the Research Grants Council of Hong Kong SAR (Project: CityU 100804) and a strategic research grand from City University of Hong Kong (Project: 7002107).

References

[1] A. M. Samsonov, Nonlinear strain waves in elastic waveguides, in: A. Jeffrey, J. Engelbrecht (Eds.), Nonlinear waves in solids, CISM Courses and Lectures, Springer, Vienna, 1994, pp. 349–382.

[2] A. V. Porubov, A. M. Samsonov, Refinement of the model for the propagation of longitudinal strain waves in a rod with nonlinear elasticity, Tech. Phys. Lett. 19 (1993) 365–366.

[3] H. Cohen, H.-H. Dai, Nonlinear axisymmetric waves in compressible hyperelastic rods: long finite amplitude waves, Acta Mech. 100 (3-4) (1993) 223–239.

[4] H. Dai, Y. Huo, Asymptotically approximate model equations for nonlinear dispersive waves in incompressible elastic rods, Acta Mech. 157 (1) (2002) 97–112.

[5] H.-H. Dai, X. Fan, Asymptotically approximate model equations for weakly nonlinear long waves in compressible elastic rods and their comparisons with other simplified model equations, Math. Mech. Solids 9 (1) (2004) 61–79.

[6] H.-H. Dai, Model equations for nonlinear dispersive waves in a compressible Mooney-Rivlin rod, Acta Mech. 127 (1-4) (1998) 193–207.

[7] H.-H. Dai, Y. Huo, Solitary shock waves and other travelling waves in a general compressible hyperelastic rod, Proc. R. Soc. Lond. A 456 (1994) (2000) 331–363.

[8] A. Constantin, W. A. Strauss, Stability of a class of solitary waves in compressible elastic rods, Phys. Lett. A 270 (3-4) (2000) 140–148.

[9] Y. Zhou, Stability of solitary waves for a rod equation, Chaos Solitons & Fractals 21 (4) (2004) 977–981.

[10] Z. Yin, On the Cauchy problem for a nonlinearly dispersive wave equation, J. Nonlinear Math. Phys. 10 (1) (2003) 10–15.

[11] G. M. Coclite, H. Holden, K. H. Karlsen, Global weak solutions to a generalized hyperelastic-rod wave equation, SIAM J. Math. Anal. 37 (4) (2005) 1044–1069.

[12] R. Ivanov, On the integrability of a class of nonlinear dispersive wave equations, J. Nonlinear Math. Phys. 12 (4) (2005) 462–468.

[13] R. Camassa, D. D. Holm, An integrable shallow water equation with peaked solitons, Phys. Rev. Lett. 71 (1993) 1661–1664.

[14] B. Fornberg, A practical guide to pseudospectral methods, Cambridge University Press, Cambridge, 1996.

[15] A. Salupere, J. Engelbrecht, P. Peterson, On the long-time behaviour of soliton ensembles, Math. Comput. Simulation 62 (1-2) (2003) 137–147.

[16] P. G. Ciarlet, Mathematical elasticity, North-Holland Publishing Co., Amsterdam, 1988.

[17] P. Haupt, Continuum mechanics and theory of materials, Springer-Verlag, Berlin, 2000.

[18] R. Hill, Aspects of invariance in solid mechanics, in: Advances in applied mechanics, Vol. 18, Academic Press, New York, 1978, pp. 1–75.

[19] A. V. Porubov, Amplification of Nonlinear Strain Waves in Solids, World Scientific, Singapore, 2003.

[20] C. Christov, M. Velarde, Dissipative solitons, Physica D 86 (1995) 323–347.

[21] I. Kliakhandler, A. Porubov, M. Velarde, Localized finite-amplitude disturbances and selection of solitary waves, Physical Review E 62 (4) (2000) 4959–4962.

[22] A. V. Porubov, V. V. Gursky, G. A. Maugin, Selection of localized nonlinear seismic waves, Proc. Estonian Acad. Sci. Phys. Math. 52 (1) (2003) 85–93.